# Controlling surface defects and photophysics in $TiO_2$ nanoparticles

Manuel J. Llansola-Portoles[§]*, Jesse J. Bergkamp[§], Daniel Finkelstein-Shapiro[§], Benjamin D. Sherman[§], Gerdenis Kodis[§], Nada M. Dimitrijevic[†], Devens Gust[§], Thomas A. Moore[§], Ana L. Moore[§].

[§]Department of Chemistry and Biochemistry, Center for Bioenergy and Photosynthesis, Arizona State University, Tempe, Arizona 85287-1604, USA. *e-mail: mjllansola@asu.edu

[†]Argonne National Laboratory, Chemical Sciences and Engineering Division and Center of Nanoscale Materials, 9700 S. Cass Ave. Argonne, IL 60439, USA.

***Corresponding Author***

*Manuel J. Llansola-Portoles. e-mail: mjllansola@asu.edu

KEYWORDS: surface defects, $Ti^{3+}$, electron transfer, perylenes, dye-sensitized solar cell, optical properties.

**ABSTRACT**

Titanium dioxide ($TiO_2$) is widely used for photocatalysis and solar cell applications, and the electronic structure of bulk $TiO_2$ is well understood. However, surface structure of nanoparticulate $TiO_2$, which has a key role in properties such as solubility and catalytic activity, still remains controversial. Detailed understanding of surface defects structures may help explain reactivity and overall materials performance in a wide range of applications. In this work we address the solubility problem and surface defects control on $TiO_2$ nanoparticles. We report the synthesis and characterization of ~ 4 nm $TiO_2$ anatase spherical nanoparticles that are soluble and stable in a wide range of organic solvents and water. By controlling the temperature during the synthesis, we are able to tailor the density of defect states on the surface of the $TiO_2$ nanoparticles without affecting parameters such as size, shape, core crystallinity and solubility. The morphology of both kinds of nanoparticles was determined by TEM. EPR experiments were used to characterize the surface defects, and transient absorption measurements demonstrate the influence of the $TiO_2$ defect states on photoinduced electron transfer dynamics.

## INTRODUCTION

Titanium dioxide ($TiO_2$) has long been a workhorse of artificial solar energy research. It was used in the first photocatalytic water splitting device,[1] in electrodes in dye-sensitized solar cells[2], in bio-inorganic systems[3] and as the semiconductor of choice for environmental remediation applications.[4-7] It owes its success to its high stability, non-toxicity, adequate alignment of its energy bands edges and particular defect structure which endows it with highly reactive sites.[8] The electronic structure of bulk $TiO_2$ is now well understood,[7-8] whereas the structure and properties of the surface remain controversial.[8-9] The $TiO_2$ surface consists of high-energy bond configurations in which the terminal Ti and O atoms rearrange so that the symmetry and electronic structure of the resulting surface is different from that of the bulk[10] creating states that would be considered defects in the bulk material. These defect states are composed of undercoordinated $Ti^{4+}$ sites resulting from surface curvature, and oxygen vacancies resulting in $Ti^{3+}$ sites.[11] Surface defects influence the interfacial charge-transfer kinetics,[12-13] modify the reactivity in catalytic processes[14] and affect the gas-adsorption distribution constants (CO, $CO_2$, $H_2$, and $H_2O$).[15] The energy levels resulting from changes in the electronic structure of reconstructed surface species are found in the mid-bandgap region.[16] The diversity of exposed facets, surface terminations and defect types present within a given polymorph of $TiO_2$ (anatase, rutile and brookite) give rise to radically different behavior.[8] Defects in the $TiO_2$ surface act as both anchoring sites and charge injection/recombination sites and thereby play a crucial role in the electron injection and recombination dynamics of the material.[5,11,17] In addition to controlling the surface reactivity, the defects may affect the electronic structure in a significant fraction of

the atoms of $TiO_2$. For example, in a 4 nm $TiO_2$ particle roughly 31% of the atoms are on the surface.[18]

There are several methods used for creating surface defects in $TiO_2$: UV radiation,[19] annealing in vacuum,[20] ion sputtering,[20] plasma-treating[21] and controlling the calcination atmosphere during synthesis.[15] Unfortunately, these methods affect not only surface properties, but also size, shape, and crystallinity of nanoparticles. Several low-temperature techniques for synthesizing $TiO_2$ nanoparticles have been developed using the following approaches: sol-gel methods,[22] formation from Ti-alkoxide precursors in aqueous[23] or organic media,[24] $TiCl_4$ hydrolysis at low temperature,[25] and a non-hydrolytic combination of Ti-alkoxide and $TiCl_4$.[26] However, these methods have given rise to issues such as controlling the reaction rates which lead to the loss of microstructural control[22] and obtaining nanoparticles which are not soluble in organic solvents. Therefore, in order to perform experiments in different media than water, their dispersion can only be achieved by constructing a complex system involving reverse micelles which have intrinsic problems such as surface crowding, micelle-chromophore interactions and excess free micelles in solution.[27] The method described in this manuscript presents the possibility of controlling the density of surface defects on the nanoparticles and allows to use $TiO_2$ nanoparticles without micelles in non-aqueous environments, expanding the available conditions for device optimization and for some applications for which organic solvent is required.[2]

Herein, we report a strategy for obtaining small $TiO_2$ anatase nanoparticles, which offers advantages due to their solubility in a wide range of organic solvents and water. By carrying out the procedure in the presence of organic solvent, the surface becomes terminated by methyl

groups covalently bound to the lattice, making these nanoparticles, to the best of our knowledge, the first micelle-free $TiO_2$ nanoparticles highly soluble in organic solvents, as well as water. The resulting nanoparticles are stable over long periods of time, and can be dried and redispersed in the solvent of choice without the irreversible aggregation typical of other $TiO_2$ nanoparticules. Furthermore, we demonstrate control over the surface defect density while keeping parameters such as the number of methyl groups on the surface, size, shape and crystalline phase essentially constant, producing nanoparticles which span the range from minimal surface defects to highly defective (with red-shifted absorption). The transient absorption experiments highlight the big role that the surface defects plays on charge transfer dynamics. Hence, our system opens the possibility of exploring the interaction of defects with sensitizers in a variety of solvents in colloidal suspension.

## EXPERIMENTAL SECTION

***Materials.*** Titanium tetrachloride (≥97.0%), dichloromethane (anhydrous, 99.5%), acetonitrile (anhydrous 99.9%) and methanol (anhydrous 99.8%) were purchased from Sigma-Aldrich and used as received.

***High Resolution Transmission Electron Microscopy***. TEM micrographs were obtained using a Philips CM200 TEM at 200kV, Cs 1.2 mm, PTP Resolution: 0.25nm Focused Probe: 0.5nm and Imaging Modes: TEM/STEM. TEM micrographs were analyzed using Digital Micrograph™ software[28]

***Electron Paramagnetic Resonance***. Continuous wave electron paramagnetic resonance (CW-EPR) spectra were acquired with a Bruker Elexsys E580 spectrometer equipped with an Oxford

CF935 helium flow cryostat with an ITC-5025 temperature controller. Samples were placed into a quartz EPR tube and bubbled with argon for 15 min to remove air/oxygen. Excitation of the sample in the EPR spectrometer was carried out with a broadband Xenon lamp equipped with water as an IR cut-off filter.

***Steady state absorption***. Spectra were recorded in 1.0 cm path length cuvette with the following spectrophotometers: Steady-state absorption spectra were measured on a Shimadzu UV2550 UV-visible spectrometer.

***Spectroelectrochemical experiments***. Spectroelectrochemical experiments were conducted using 1 cm quartz cuvettes under a constant Ar flow, a Shimadzu UV-3101PC spectrophotometer, and a CH Instruments 650C potentiostat. An indium doped tin oxide (ITO) working electrode, $Ag^+/Ag$ quasi-reference electrode, and platinum wire counter electrode were set inside the quartz cuvette. Approximately 0.4 mL of dichloromethane containing 100 mM $TBAPF_6$ and dye was added to the cuvette, and the solution level was maintained during the experiment by addition of neat dichloromethane to account for evaporative losses. Attachment of a glass cover slip over the conductive face of the ITO with heat-shrink plastic allowed the cavity between the ITO and cover slip to fill by capillary action when the sample was immersed in solution, and thereby provided a small volume of analyte on the working electrode. The beam of the spectrophotometer was manipulated to measure only the solution contained in the working electrode and the small volume ensured bulk electrolysis of the solution in the path length during the course of the experiment. The absorbance spectrum of the singly oxidized form of perylene dye was measured by applying positive potential (determined by a prior CV scan of the setup) for 15 min.

***Time resolved absorption***. Femtosecond to nanosecond transient absorption measurements were acquired with a kilohertz pulsed laser source and a pump-probe optical setup. Laser pulses at 800 nm (c.a. 100 fs) were generated from an amplified, mode-locked titanium sapphire kilohertz laser system (Millennia/Tsunami/Spitfire, Spectra Physics). Part of the laser pulse energy was sent through an optical delay line and focused onto a 3 mm sapphire plate to generate a white light continuum for the probe beam. The remainder of the pulse energy was used to pump an optical parametric amplifier (Spectra Physics) to generate excitation pulses at 650 nm, which were selected using a mechanical chopper. The white light generated was compressed by prism pairs (CVI) before passing through the sample. The polarization of the pump beam was set to the magic angle (54.7°) relative to the probe beam and its energy was adjusted to 200 nJ using a continuously variable neutral density filter. The beams were focused in a 2 mm path-length quartz cuvette to a ~200 μm diameter spot. The white light probe was dispersed by a spectrograph (300 line grating) onto a charge-coupled device (CCD) camera (DU420, Andor Tech.). The final spectral resolution was about 2.3 nm for over a nearly 300 nm spectral region. The instrument response function was ca. 100 fs. Perylene-$TiO_2$ systems were dissolved in acetonitrile to an absorbance of 0.8 at the excitation wavelength in 2 mm path-length cuvette. The decay-associated spectra (DAS) were obtained by fitting globally the transient absorption kinetic traces over a selected wavelength region simultaneously as described by equation (1) (parallel kinetic model).[29]

$$\Delta A(\lambda,t) = \sum_{i=1}^{n} A_i(\lambda)\exp(-t/\tau_i) \qquad (1)$$

where $\Delta A(\lambda,t)$ is the observed absorption change at a given wavelength at time delay $t$ and $n$ is the number of kinetic components used in the fitting. A plot of $A_i(\lambda)$ versus wavelength is called a Decay Associated Spectra (DAS) and represents the amplitude spectrum of the $i^{th}$ kinetic component, which has a lifetime of $\tau_i$. Random errors associated with the reported lifetimes obtained from transient absorption measurements were typically ≤ 5%. Rigorous analysis of absorption data in a non-homogeneous system requires the use of a model which considers a distribution of multi-exponential decays to describe the kinetics of each transient species and thus accounting for the distribution of available environments in the heterogeneous system. In our analysis we used the minimum number of exponential components for an adequate fitting of the experimental data within the experimental error. Thus it is possible that the reported decay components correspond to a weighted mean value of the actual distribution of constants associated with each species.

## RESULTS AND DISCUSSION

The nanoparticles were prepared in argon atmosphere using 80 mL of dichloromethane as a solvent. It was kept at 195 K for the preparation of $TiO_2$ nanoparticles with low density of defect states (L-$TiO_2$) and at 313 K for $TiO_2$ nanoparticles with high density of defect states (R-$TiO_2$). Under continuous stirring, 200 μL of $TiCl_4$ were introduced into the reactor and 3 mL of methanol were added dropwise and allowed to react for 2 h. The synthesis of both L-$TiO_2$ and R-$TiO_2$ follow identical steps with the exception of the reaction temperature (see supporting information). The morphologies of L-$TiO_2$ and R-$TiO_2$ were studied by high resolution transmission electron microscopy (HRTEM). Figure 1 shows nearly spherical particles with the

size distribution presented in the inset histogram. Fitting the size distribution to a Gaussian model, mean diameters of 3.8 nm (FWHM = 1.3 nm) and 3.7 nm (FWHM = 1.7 nm) for L-$TiO_2$ and R-$TiO_2$ were obtained, respectively. Although both samples have the same average size; R-$TiO_2$ particles have a larger size dispersion, which we attribute to the faster reaction rate during the preparation, which does not allow the nanoparticles to grow as uniformly as they do at lower temperature. Lattice planes were determined analyzing the profile of the nanoparticles of HRTEM images in Figure 1 (profiles shown in supporting information). For both kinds of nanoparticles lattice planes of 1.6 ± 0.1 Å and 2.4 ± 0.1 Å were found, which matches the literature values of 1.6 Å and 2.4 Å reported for the (211) and (004) planes of tetragonal anatase.[30-32] Confirmation that anatase is the crystalline phase for both R-$TiO_2$ and L-$TiO_2$ nanoparticles was demonstrated by TEM results, EPR measurements and UV-vis spectra (*vide infra).* Such results are in agreement with the observations of Durupthy and co-workers who showed that anatase is the most stable phase for $TiO_2$ nanoparticles smaller than 14 nm.[33]

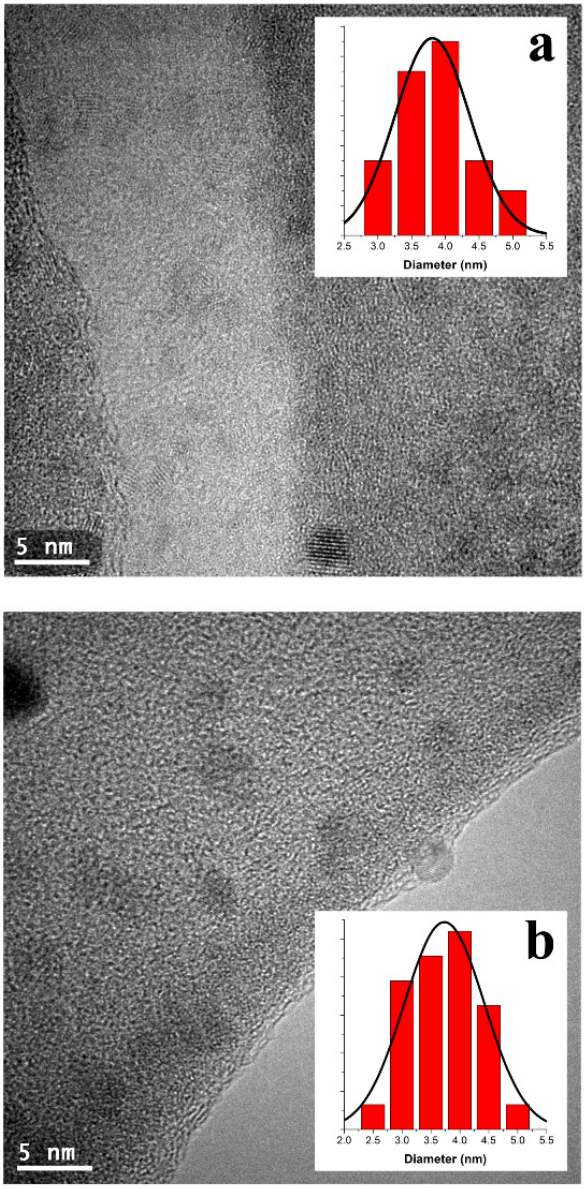


***Figure 1:*** *HRTEM micrographs of $TiO_2$ nanoparticles* ***a)*** *High magnification image showing crystallinity in the L-$TiO_2$.* ***Inset:*** *Histogram of size distribution and Gaussian fit (black line).* ***b)*** *High magnification image showing crystallinity in the R-$TiO_2$.* ***Inset:*** *Histogram of the size distribution and Gaussian fit (black line).*

Figure 2 shows the UV-Vis absorption spectra of R-$TiO_2$ and L-$TiO_2$ at a concentration of 250 mg/mL in acetonitrile. The band gap energy was determined using equation (2),[34] (Tauc plot; inset Figure 2) where $\boldsymbol{\alpha}$ is the absorption coefficient, $\boldsymbol{k}$ is a constant, $\boldsymbol{h}$ is Planck's constant, $\boldsymbol{\upsilon}$ represents the frequency of incident light and $\boldsymbol{E_g}$ is the band gap energy in electron volts.

$$(\alpha h\upsilon)^2 = k(h\upsilon - E_g) \qquad (2)$$

The value obtained (3.25 ± 0.05) eV is the same for R-$TiO_2$ (red dots) and L-$TiO_2$ (black dots), indicating that the core of both samples is crystalline phase anatase with no appreciable size-based quantum effects.[8,35-37] L-$TiO_2$ shows negligible light absorption at energies lower than the band gap energy, suggesting a low density of defect states, whereas R-$TiO_2$ exhibits a strong absorption in the region from 400 nm to 650 nm, which is attributed to transitions involving defect states at the surface. Indeed, band gap absorption ($\lambda < 400$ nm) remains constant for all solvents whereas the characteristics of absorption attributed to defect states (400 nm $< \lambda <$ 650 nm) depend on the surrounding solvent. This behavior strongly suggests that the band gap absorption is due to the anatase core (not in contact with the solvent), whereas the absorption due to defect states arises in solvent-contacted surface regions (see Supporting Information, Figure S7).

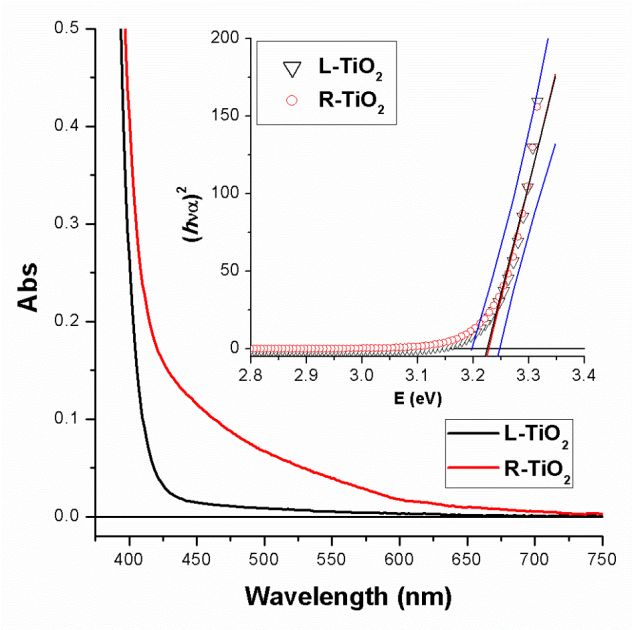


***Figure 2:*** *Absorption spectra of L-$TiO_2$ (black line) and R-$TiO_2$ (red line) in acetonitrile at a concentration of 250 mg/mL.* ***Inset:*** *Absorption onset value of the first direct allowed transition for L-$TiO_2$ (black line) and R-$TiO_2$ (red line). Intersection of the lines on the x axis at y = 0 indicates the estimated band gap energy and blue lines represent the confidence bands of 99% for the fitting using equation (2).*

Continuous wave electron paramagnetic resonance (CW-EPR) measurements were carried out at 4.5 K to characterize the structure and nature of the paramagnetic centers created in R-$TiO_2$ and L-$TiO_2$ upon UV-vis irradiation. The EPR spectrum for nanoparticles without illumination reveals the presence of $Ti^{3+}$ and oxygen vacancies on the surface of R-$TiO_2$, which are absent in L-$TiO_2$ (Figure 3a). This supports the observation from UV-vis spectroscopy that R-$TiO_2$ nanoparticles have indeed a higher density of defect states. Under UV-vis illumination we find that the photogenerated charges localize on the surface in both type of nanoparticles. Oxidizing equivalents exist as oxygen-centered radicals, ($Ti^{4+}$-$O^{\bullet}$) and reducing equivalents as

$Ti^{3+}$ centers (Figure 3b). The g-tensors of photogenerated charges ($g_z$ = 2.041, $g_y$ = 2.012, $g_x$ = 2.002 for O-centered radicals and g = 1.9344 for $Ti^{3+}$ for L-$TiO_2$, and $g_z$ = 2.047, $g_y$ = 2.016, $g_x$ = 2.002 for O-centered radicals and g = 1.9071 for $Ti^{3+}$ for R-$TiO_2$) agree with those of an anatase structure. The trapping of electrons on the surface at 4.5 K is characteristic of anatase particles with small domains of crystallinity and/or a high density of five-coordinated surface $Ti^{4+}$ that are formed as a result of high curvature of the nanoparticles.[38-39] These undercoordinated sites preferentially act as electron traps on the surface and become reduced to the paramagnetic center $Ti^{3+}$. Normalizing the signals to the oxygen-centered radicals clearly shows that the density of photoexcited $Ti^{3+}$ centers (arising from reduced uncoordinated $Ti^{4+}$ on the surface) is larger for R-$TiO_2$ than L-$TiO_2$. The double integral of the CW-EPR spectrum normalized to the value of the oxygen radical signal indicates that the concentration of photoexcited states in R-$TiO_2$ is 34% higher than in L-$TiO_2$. Moreover, the presence of oxygen vacancies at the surface of R-$TiO_2$ affects the overall electron density distribution, as seen in different g-tensor values for photogenerated charges localized on the surface of L-$TiO_2$ and R-$TiO_2$. It is likely that these oxygen vacancies stabilize a larger number of undercoordinated $Ti^{4+}$ in R-$TiO_2$.

To further study the surface, we examined the adsorption of the superoxide anion and perylene dye (*vide infra*) on both kinds of nanoparticles.[38-39] The superoxide anion is created by exposure of the nanoparticles to ozone for five h. The observed superoxide anion exhibits g-tensor values of $g_z$=2.0217, $g_y$=2.0091, $g_x$=2.0024 for R-$TiO_2$ and $g_z$=2.0193, $g_y$=2.0091, $g_x$=2.0024 for L-$TiO_2$ (Figure 3c).[39-41] Superoxide anion ($O_2^-$) is a 13-electron $\pi$ radical characterized by the presence of three electrons in two $2\pi^*$ antibonding orbitals. Despite the presence of an unpaired electron in this radical, the CW-EPR spectrum is only observed when the degeneracy of both $\pi^*$ orbitals

is removed by external perturbations, such as an external electric field. The splitting (ΔE) of the π* levels determines the value of the $g_z$ component ($g_z = g_e + 2\lambda/\Delta E$). Thus the $g_z$ value depends on the nature of the adsorption site and its local electric field. The difference observed for the values of the $g_z$ component confirms different local environments at the surface for the R-$TiO_2$ and L-$TiO_2$ nanoparticles.[38,40-42] The system dye–R-$TiO_2$ shows evidence of charge transfer (CT) complex[43] formation, whereas dye–L-$TiO_2$ does not, suggesting the presence of strong electronic coupling between near-by defects and the dye in the dark (see Supporting Information Figure S6).

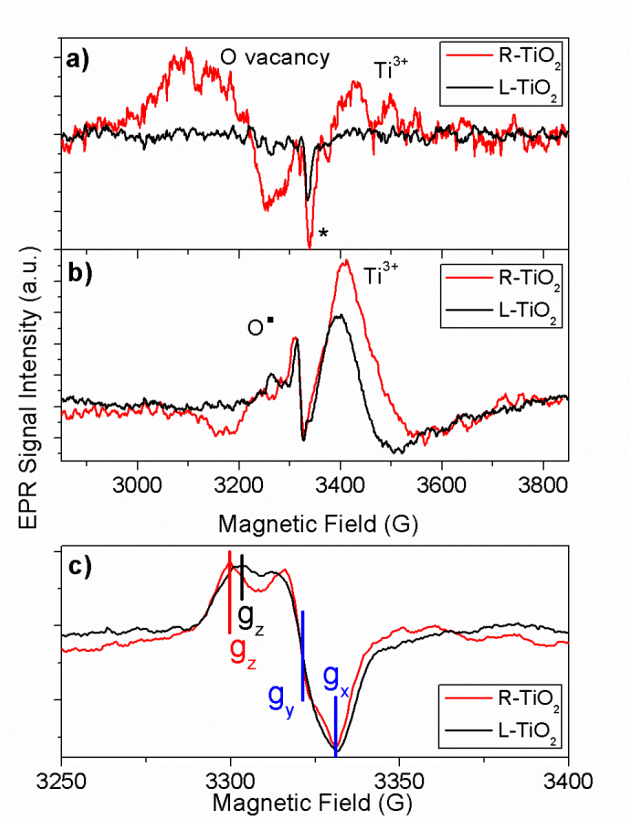


***Figure 3. a)*** *Dry L-$TiO_2$ and R-$TiO_2$ in the dark. We observe the presence of oxygen vacancies and $(Ti^{3+})_{surf}$ centers in R-$TiO_2$. The sharp feature (*) is an artifact of the cavity signal*

*subtraction.* ***b)*** *CW-EPR of dry L-$TiO_2$ and R-$TiO_2$ upon UV illumination. Both oxygen centered radicals, ($Ti^{4+}$-$O^{\bullet}$), and surface $(Ti^{3+})_{surf}$ radicals are observed. Spectra are normalized to the oxygen radical signal.* ***c)*** *CW-EPR of adsorbed superoxide on R-$TiO_2$ and L-$TiO_2$ in the dark. Superoxide is obtained by exposing the surface to ozone for five hours.*

In order to determine the role of defect states in photoinduced electron transfer processes, a perylene dye bearing a phosphonic acid group as a binding moiety (*dye* in Scheme 1) was synthesized and attached to the surface of the nanoparticles.[44] Scheme 1 depicts the relative energetics for the oxidation of the ground and excited states of the dye, the conduction band edge (CB), valence band edge (VB) and defect state energy levels of $TiO_2$.[45] The potential of the defect states of $TiO_2$ were calculated using the UV-vis absorption spectra of R-$TiO_2$ in acetonitrile. The potential for the first oxidation ($D^{\bullet+}/D$) of the dye was measured electrochemically (Supporting Information, Figure S5). The potential for the oxidation of the excited state ($D^{\bullet+}/D^*$) was calculated with the equation $D^{\bullet+}/D^* = D^{\bullet+}/D - E_{00}$, where $E_{00}$ is the zero-zero optical excitation energy estimated from the intersection of the normalized absorption and emission spectra in acetonitrile (Supporting information, Figure S8).

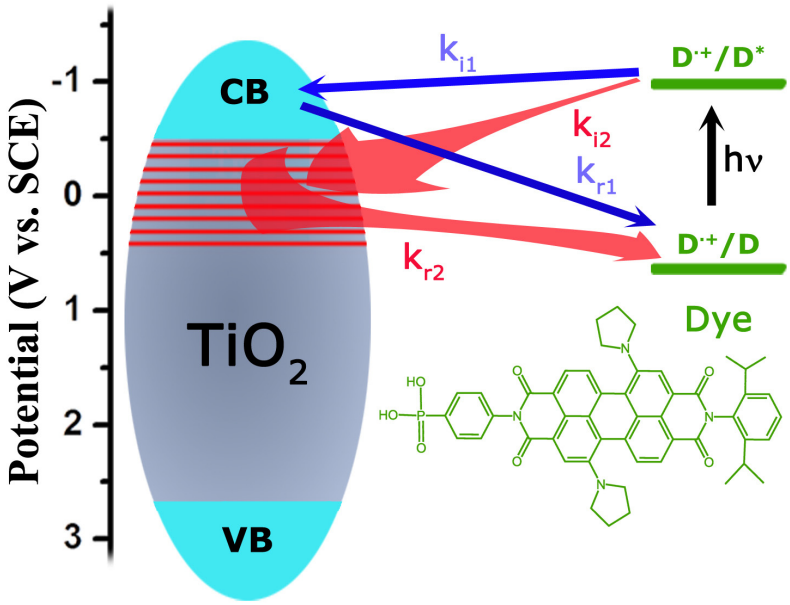


***Scheme 1.*** *Diagram depicting the potentials for the ground and the lowest excited singlet states of the perylene dye, $TiO_2$ conduction band energy (CB), $TiO_2$ valence band energy (VB) and $TiO_2$ energy levels due to defect states (red lines). Broad arrows indicate that electrons can be injected from the exited state of the dye into different trap states and that electrons can recombine from different trap states into the ground state of the oxidized dye.*

As shown in Scheme 1, the excited singlet dye species is thermodynamically capable of photoinjecting an electron into the conduction band and/or defect states of $TiO_2$. Theoretical work affirms that defect states may act as electron acceptors and thereby increase the driving force for the photoinduced electron transfer process.[46-47] Nevertheless, there are no experimental studies comparing the dynamics of the electron transfer processes in cases where the density of defect states is the only variable in the system. It is expected that for L-$TiO_2$, the CB is the most probable electron-accepting energy level and electron transfer would follow the pathway

depicted by the blue arrows in Scheme 1: injection from the excited dye into the CB and recombination from the CB to the oxidized dye. For R-$TiO_2$, electron injection can take place into both CB, indicated by the blue arrow, and into a wide distribution of defect states as indicated by the red broad arrow.

Femtosecond transient absorption experiments were performed to explore the role of defect states in the kinetics of the photoinduced electron transfer reactions in the dye–$TiO_2$ systems in acetonitrile solution. The global analysis of transient absorption decay kinetics for the dye alone (Figure 4a) gives two decay-associated spectra (DAS) with lifetimes of 1.6 ps and 1036 ps. The 1036 ps DAS shows negative amplitudes at around 700 and 770 nm corresponding to the ground state bleaching and stimulated emission of the dye, respectively; therefore it can be assigned to the decay of the singlet excited state. The 1.6 ps DAS shows a shift of the stimulated emission band from about 730 nm (negative amplitude) to 780 nm (positive amplitude). This DAS can be assigned to solvation (relaxation) of the excited state of the dye. Inset 5a shows the difference absorption spectrum of the singly-oxidized dye cation radical ($dye^{\bullet+}$) obtained by spectroelectrochemistry of the dye free in solution. It has strong induced absorption on both sides of the ground state bleaching (~ 700 nm) of the dye.

The global analysis of the transient absorption data for the dye-associated L-$TiO_2$ (Figure 4b) gives four DAS with lifetimes of ~200 fs, 5 ps, 65 ps and 463 ps. The 200 fs DAS can be attributed to electron injection from the singlet excited state of the dye into the conduction band of the L-$TiO_2$. It shows the decay of stimulated emission around 720-800 nm and simultaneously the formation of dye radical cation indicated by the $dye^{\bullet+}$ absorption characteristics presented

around 540-600 nm (see 4a inset). The 5 ps DAS is similar to the difference absorption spectrum of the $dye^{\bullet+}$ obtained by spectroelectrochemistry in solution and therefore can be attributed to the recombination of the charge separated state that was formed with a time constant of 200 fs. The 65 ps DAS shows positive amplitudes around 610 and 720 nm, these features are not characteristics of the $dye^{\bullet+}$ however this DAS can be attributed to dye solvation (relaxation) and cooling after very fast (5 ps) ground state recovery. For the 65 ps DAS, the ground state solvation can be attributed to the blue shift of ground state bleaching (observed negative amplitude at 690 nm and positive amplitude at 610 nm) and the ground state cooling can be attributed to induced absorption from the ground state at wavelengths characteristic of the stimulated emission (observed positive amplitude at 720 nm). The 463 ps DAS can be attributed to the decay of the singlet excited state of the weakly attached (physisorbed) and aggregated dye. It shows ground state bleaching, stimulated emission, and featureless induced absorption below 620 nm due to absorption by the singlet excited state which is similar to that observed for the free dye in solution (1036 ps DAS, Figure 4a). The $dye^{\bullet+}$–$TiO_2(e^-)$ formation and recombination can also be followed by the characteristic induced absorption at 990 nm due to the free carriers (injected electrons) in the $TiO_2$ semiconductor [48] (see Supporting Information, Figure S7). It should be emphasized that because of strong dye–$TiO_2$ system heterogeneity the observed DAS cannot be attributed to pure transient species and can have contributions from other species decaying with the same lifetime. For example, the 5 ps DAS most likely has some contribution from the physisorbed dye excited state solvation observed for the dye alone in solution and the 463 ps DAS has some contribution from the dye ground state relaxation and possibly from some species that undergo slower charge separated state recombination.

The global analysis of the transient absorption for the dye–R-$TiO_2$ (Figure 4c) gives a satisfactory fit with five decay lifetimes of ~100 fs, 1.5 ps, 11 ps, 228 ps and a component that does not decay within the 3.5 ns measurement time window. The dye–R-$TiO_2$ system shows even higher heterogeneity. The ~100 fs DAS can be attributed to the formation of charge separated states involving the $TiO_2$ CB and shallow defect states. Induced absorption at the blue and red edges of the spectrum shows that some charge separation already happened on a much faster time scale, presumably involving the lower energy (deeper) defect states, with more driving force. The 11 ps, 228 ps and nondecaying DAS are associated with recombination of charge separated species. The 1.5 ps DAS most likely shows the excited state solvation of the weakly attached dye as was observed for the free dye in solution (Figure 4a). However the negative amplitude around 590 nm it must also have some contribution from species which form charge separated state on a slower time scale, presumably from weakly coupled species at specific defect sites. The 228 ps DAS apart from features characteristic of the charge separated state as observed in the nondecaying DAS, which corresponds to the pure charge separated species, has features characteristic of the dye ground state solvation and cooling as was observed for the dye–L-$TiO_2$ system. In addition, it has a contribution from the singlet excited state decay of physisorbed aggregated dye (negative amplitude due to stimulated emission at ~780 nm).

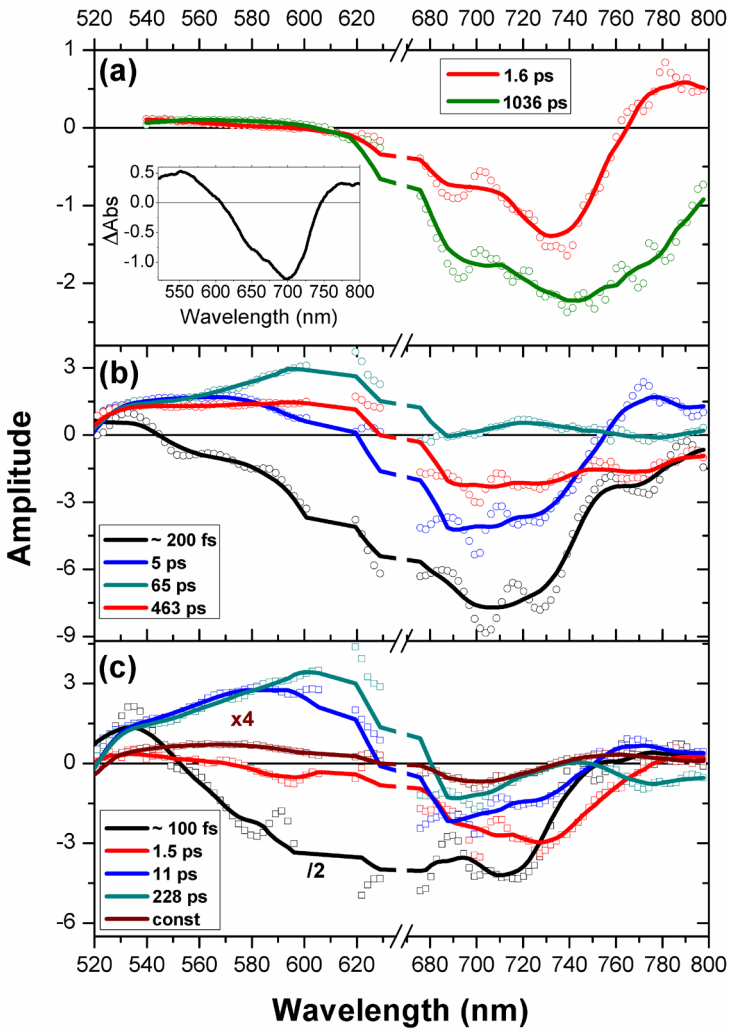


***Figure 4.*** *Decay-associated-spectra in acetonitrile solution measured by fs transient absorption upon excitation at 650 nm for* ***a)*** *dye,* ***b)*** *dye–L-$TiO_2$,* ***c)*** *dye–R-$TiO_2$.* ***Inset****: spectroelectrochemical difference spectrum in dichloromethane showing the difference in absorption of the singly oxidized form of dye from its neutral ground state form.*

The overall transient absorption results discussed above show evidence that dye–L-$TiO_2$ and dye–R-$TiO_2$ systems both undergo photoinduced electron transfer to yield the species $dye^{\bullet+}$–L-$TiO_2(e^-)$ and species $dye^{\bullet+}$–R-$TiO_2(e^-)$. The apparent forward ($k_{i1}$) and reverse ($k_{r1}$) rate constants

for the formation and decay of the dye$^{\bullet+}$–L-$TiO_2$($e^-$) state can be estimated as $k_{i1} \sim 5 \times 10^{12}$ $s^{-1}$ (1/200 fs) and $k_{r1} \sim 2 \times 10^{11}$ $s^{-1}$ (1/5 ps), respectively. The apparent forward and reverse rate constants for the formation and decay of the dye$^{\bullet+}$–R-$TiO_2$($e^-$) state are difficult to estimate because of the heterogeneity of the system, nevertheless the rates can be roughly approximated as $k_{i2} \sim 1 \times 10^{13}$ $s^{-1}$ (1/100 fs), $k_{r2} \sim 9.1 \times 10^{10}$ $s^{-1}$ (1/ 11 ps (50%)) and $k_{r2} \sim 4.4 \times 10^{9}$ $s^{-1}$ (1/ 228 ps (46%)), respectively (there is some even slower recombination, 4%, associated most likely with some deeply trapped electrons). The faster injection for dye–R-$TiO_2$ than for dye–L-$TiO_2$ could be explained by the larger driving force, the larger density of states and stronger electronic coupling at the defect sites (as shown in EPR measurements Figure S6, Supporting Information). Stronger electronic coupling has been observed in other nanoparticulated $TiO_2$ systems.[49] This electronic coupling possibly results in the formation of charge transfer excitons which facilitate injection into the CB and/or distant defect states. Recombination is slower for the dye–R-$TiO_2$ because the electron can escape from the initially formed charge separated state (CT exciton) and migrate into other surface defect states, where it eventually gets trapped. This effect is consistent with the well-known slower mobility of electrons in trap states than in the CB.[50] On the other hand, for dye–L-$TiO_2$ the electrons have higher mobility in the conduction band and are more readily available to recombine. The presence of a higher density of defect states leads to a tighter coupling of the dye with the surface, increases the density of accepting states with larger driving force for electron injection, and therefore facilitates injection and helps to stabilize the charge separated state.

## CONCLUSIONS

We are reporting a method for the preparation of $TiO_2$ nanoparticles, which form stable suspensions in a wide range of organic solvents at concentrations up to 250 mg/mL. By controlling the temperature during synthesis, these 3-5 nm diameter $TiO_2$ nanoparticles can be prepared with either a high or a low density of defect states without affecting parameters such as size, shape, core crystallinity and solubility. Due to the ability to control the defect states and the excellent optical properties in a variety of organic solvents and water, these materials provide a good platform for studies of photoinduced electron transfer reactions at interfaces. The important role of surface defects in electron transfer dynamics has been proved. We show that there is a well-marked difference in the behavior of the electron transfer dynamics as a function of the density of defect sites. When the density of surface defects is low the electron follow a single injection/recombination pathway. However, in high density surface defects nanoparticles there are multiple injection paths and several recombination rates depending on the stabilization effect of the surface trap on the charge separated state.

## ACKNOWLEDGEMENTS

The work at ASU was supported by the Center for Bio-Inspired Solar Fuel Production, an Energy Frontier Research Center funded by the U.S. Department of Energy, Office of Science, Office of Basic Energy Sciences under Award Number DE-SC0001016, National Science Foundation CHE-1124895 and the research at ANL was supported by the Department of Energy, Office of Science, Office of Basic Energy Sciences, under Contract No DE-AC02-06CH11357.

## ASSOCIATED CONTENT

*Supporting information* includes a reaction mechanism for formation of $TiO_2$ nanoparticles, FTIR-ATR, TEM latice fringes profiles, thermogravimetry, perylene dye synthesis and characterization, binding of perylene mechanism to $TiO_2$, electron paramagnetic resonance experiments with dye binded to $TiO_2$ and extended photophysical characterization. “This material is available free of charge via the Internet at http://pubs.acs.org.” ko

## AUTHOR INFORMATION

### *Corresponding Author*

*To whom correspondence should be addressed to: mjllansola@asu.edu

### *Notes*

The authors declare no competing financial interest.

## REFERENCES

(1) Fujishima, A.; Honda, K. *Nature* **1972**, *238*, 37.
(2) O'regan, B.; Grätzel, M. *Nature* **1991**, *353*, 737.
(3) Mershin, A.; Matsumoto, K.; Kaiser, L.; Yu, D.; Vaughn, M.; Nazeeruddin, M. K.; Bruce, B. D.; Graetzel, M.; Zhang, S. *Scientific Reports* **2012**, *2*.
(4) Fujishima, A.; Zhang, X. *C. R. Chim.* **2006**, *9*, 750.
(5) Linsebigler, A. L.; Lu, G.; Yates, J. T. *Chem. Rev. (Washington, DC, U. S.)* **1995**, *95*, 735.
(6) Fujishima, A.; Rao, T. N.; Tryk, D. A. *J. Photochem. Photobiol., C* **2000**, *1*, 1.
(7) Hoffmann, M. R.; Martin, S. T.; Choi, W.; Bahnemann, D. W. *Chem. Rev. (Washington, DC, U. S.)* **1995**, *95*, 69.
(8) Diebold, U. *Surf. Sci. Rep.* **2003**, *48*, 53.
(9) Thompson, T. L.; Yates, J. T. *Chem. Rev. (Washington, DC, U. S.)* **2006**, *106*, 4428.
(10) Diebold, U. *Nat. Mater.* **2010**, *9*, 185.
(11) Vijayan, B.; Dimitrijevic, N. M.; Rajh, T.; Gray, K. *J. Phys. Chem. C* **2010**, *114*, 12994.

(12) Green, A. N. M.; Palomares, E.; Haque, S. A.; Kroon, J. M.; Durrant, J. R. *J. Phys. Chem. B* **2005**, *109*, 12525.
(13) Gregg, B. A.; Chen, S.-G.; Ferrere, S. *J. Phys. Chem. B* **2003**, *107*, 3019.
(14) Gong, X.-Q.; Selloni, A.; Batzill, M.; Diebold, U. *Nat. Mater.* **2006**, *5*, 665.
(15) Suriye, K.; Praserthdam, P.; Jongsomjit, B. *Appl. Surf. Sci.* **2007**, *253*, 3849.
(16) Gutierrez, C.; Salvador, P. *J. Electroanal. Chem. Interfacial Electrochem.* **1982**, *138*, 457.
(17) Hurum, D. C.; Agrios, A. G.; Gray, K. A.; Rajh, T.; Thurnauer, M. C. *J. Phys. Chem. B* **2003**, *107*, 4545.
(18) Chen, L. X.; Rajh, T.; Wang, Z.; Thurnauer, M. C. *J. Phys. Chem. B* **1997**, *101*, 10688.
(19) Mezhenny, S.; Maksymovych, P.; Thompson, T. L.; Diwald, O.; Stahl, D.; Walck, S. D.; Yates Jr, J. T. *Chem. Phys. Lett.* **2003**, *369*, 152.
(20) Pan, J. M.; Maschhoff, B. L.; Diebold, U.; Madey, T. E. *J. Vac. Sci. Technol., A* **1992**, *10*, 2470.
(21) Nakamura, I.; Negishi, N.; Kutsuna, S.; Ihara, T.; Sugihara, S.; Takeuchi, K. *J. Mol. Catal. A: Chem.* **2000**, *161*, 205.
(22) Brinker, C. J.; Scherer, G. W. *Sol-Gel Science: The Physics and Chemistry of Sol-Gel Processing*; Academic Press: San Diego, 1990.
(23) Kotov, N. A.; Meldrum, F. C.; Fendler, J. H. *J. Phys. Chem.* **1994**, *98*, 8827.
(24) Skinner, D. E.; Colombo, D. P.; Cavaleri, J. J.; Bowman, R. M. *J. Phys. Chem.* **1995**, *99*, 7853.
(25) Serpone, N.; Lawless, D.; Khairutdinov, R. *J. Phys. Chem.* **1995**, *99*, 16646.
(26) Arnal, P.; Corriu, R. J. P.; Leclercq, D.; Mutin, P. H.; Vioux, A. *Chem. Mater.* **1997**, *9*, 694.
(27) Hernandez, L. I.; Godin, R. P.; Bergkamp, J. J.; Llansola-Portoles, M. J.; Sherman, B. D.; Tomlin, J.; Kodis, G.; Méndez-Hernández, D. D.; Bertolotti, S.; Chesta, C.; Mariño-Ochoa, E.; Moore, A. L.; Moore, T. A.; Cosa, G.; Palacios, R. E. *J. Phys. Chem. B* **2013**, *117*, 4568.
(28) Mitchell, D. R.; Schaffer, B. *Ultramicroscopy* **2005**, *103*, 319.
(29) Van Stokkum, I. H. M.; Larsen, D. S.; Van Grondelle, R. *Biochim. Biophys. Acta* **2004**, *1657*, 82.
(30) Zhao, X.; Jin, W.; Cai, J.; Ye, J.; Li, Z.; Ma, Y.; Xie, J.; Qi, L. *Adv. Funct. Mater.* **2011**, *21*, 3554.
(31) Anthony, J. W.; Bideaux, R. A.; Bladh, K. W.; Nichols, M. C. In *Handbook of Mineralogy*, Mineral Data Publishing: 1997; Vol. 3.
(32) Shi, J.; Sun, C.; Starr, M. B.; Wang, X. *Nano Lett.* **2011**, *11*, 624.
(33) Durupthy, O.; Bill, J.; Aldinger, F. *Cryst. Growth Des.* **2007**, *7*, 2696.
(34) Johnson, E. J. In *Optical Properties of III-V Compounds, Semiconductors and Semimetals*; R.K. Willardson, A. C. B., Ed.; Academic Press: New York, 1967; Vol. 3, p 153.
(35) Vayssieres, L.; Persson, C.; Guo, J.-H. *Appl. Phys. Lett.* **2011**, *99*.
(36) Sant, P. A.; Kamat, P. V. *Phys. Chem. Chem. Phys.* **2002**, *4*, 198.
(37) Hegazy, A.; Prouzet, E. *Chem. Mater.* **2011**, *24*, 245.
(38) Green, J.; Carter, E.; Murphy, D. M. *Chem. Phys. Lett.* **2009**, *477*, 340.
(39) Maurelli, S.; Vishnuvarthan, M.; Berlier, G.; Chiesa, M. *Phys. Chem. Chem. Phys.* **2012**, *14*, 987.

(40) Attwood, A. L.; Murphy, D. M.; Edwards, J. L.; Egerton, T. A.; Harrison, R. W. *Res. Chem. Intermed.* **2003**, *29*, 449.
(41) Berger, T.; Sterrer, M.; Diwald, O.; Knözinger, E. *ChemPhysChem* **2005**, *6*, 2104.
(42) Berger, T.; Sterrer, M.; Diwald, O.; Knözinger, E.; Panayotov, D.; Thompson, T. L.; Yates, J. T. *J. Phys. Chem. B* **2005**, *109*, 6061.
(43) Dimitrijevic, N. M.; Poluektov, O. G.; Saponjic, Z. V.; Rajh, T. *J. Phys. Chem. B* **2006**, *110*, 25392.
(44) Guerrero, G.; Mutin, P. H.; Vioux, A. *Chem. Mater.* **2001**, *13*, 4367.
(45) Grätzel, M. *Nature* **2001**, *414*, 338.
(46) Martsinovich, N.; Troisi, A. *Phys. Chem. Chem. Phys.* **2012**, *14*, 13392.
(47) Jakubikova, E.; Snoeberger Iii, R. C.; Batista, V. S.; Martin, R. L.; Batista, E. R. *J. Phys. Chem. A* **2009**, *113*, 12532.
(48) Pankove, J. I. *Optical Processes in Semiconductors*; Courier Dover Publications, 1975.
(49) Varaganti, S.; Ramakrishna, G. *J. Phys. Chem. C* **2010**, *114*, 13917.
(50) Richter, C.; Schmuttenmaer, C. A. *Nat. Nanotechnol.* **2010**, *5*, 769.

**TABLE OF CONTENTS**